Journal of Power Sources 679 (2026) 240238

Contents lists available at ScienceDirect

Journal of Power Sources

journal homepage: www.elsevier.com/locate/jpowsour

Solid-electrolyte interphase composition and homogeneity in industrial-scale Li-ion batteries – quantitative 3D tomography using AI-assisted ion beam analysis

S. Möller [a,*], Axel Durdel [b], Luiza Streck [b], K.F. Muzakka [a], M. Finsterbusch [a]

[a] Forschungszentrum Jülich GmbH, Institute of Energy Materials and Devices, Materials Synthesis and Processing (IMD-2), Jülich, 52425, Germany
[b] Technical University of Munich (TUM), TUM School of Engineering and Design, Department of Energy and Process Engineering, Chair of Electrical Energy Storage Technology (EES), Arcisstraße 21, Munich, 80333, Germany

HIGHLIGHTS

- MeV ion beam analysis tomography of 5.4 Ah Si-anode battery cell for all elements.
- 32% capacity loss after 340 cycles due to anode-side SEI formation.
- Half-cell potential shifts of ~150 mV due to changes in lithiation limits.
- 480 mAh/g_{Si} pre-lithiation optimal for compensating the Li-immobilization.
- LiF and phosphates dominate SEI with a minor fraction of Li-silicates in Si anodes.

ARTICLE INFO

Keywords:
Solid electrolyte interphase
Ion beam analysis
Material analysis
Li-ion battery
State-of-Charge
State-of-Health
Si-anodes

ABSTRACT

Si-based anodes for Li-ion batteries improve battery performance, but introduce new fatigue mechanisms, reducing their cycle-life, compared to graphite anodes. Four 110 × 80 mm^2 electrodes of a 5.4 Ah NCA + Si/G cell after 340 cycles are analysed by ion-beam analysis in 345,000 points, providing a unique insight into the degradation of the Si-anode.

Our results show an inhomogeneous state-of-charge (SoC) across the electrodes and Li immobilization at the Si-anode. After the initial formation cycling, the anode contains 10.2 atom% Li (SoC = 0), after 340 cycles this amount increases to 17.5 at.%. The F and P concentrations show most Li is immobilized as LiF. Li-silicates are only a minor fraction of the solid-electrolyte interphase, ruling them out as main driver of the accelerated degradation. The immobilized anode Li results in a cathode Li concentration drop from initially 21 at.% (SoC = 0) to 16 at.% Li after 340 cycles. This Li-loss correlates well with the aging related electrode-potential shift of 130 mV known from literature. A ±6% cathode layer thicknesses inhomogeneity is revealed through the areal density of Ni. The Li loss requires 480 mAh/g_{Si} pre-lithiation for compensating the observed Li-immobilization, which would increase cycle-life and the initial discharge capacity.

1. Introduction

In the rapidly evolving landscape of energy storage technologies, lithium-ion (Li-ion) batteries have emerged as pivotal components in a myriad of applications, ranging from portable electronics to electric vehicles and grid storage solutions. However, the efficiency, performance, longevity, and safety of these batteries are critical parameters for their application. State of Health (SoH) and State of Charge (SoC) denote the battery's condition and charge level, respectively. Understanding the underlying mechanisms resulting in certain SoH and SoC not only facilitates the optimization of battery performance and lifecycle but also enhances the reliability and safety of energy storage systems.

The SoH of a battery is indicative of its overall condition and capability to store and deliver energy. Complex electrochemical processes

This article is part of a special issue entitled: MDB 2025 : Progresses and Challenges published in Journal of Power Sources.

* Corresponding author.
E-mail address: s.moeller@fz-juelich.de (S. Möller).

https://doi.org/10.1016/j.jpowsour.2026.240238
Received 4 March 2026; Received in revised form 21 April 2026; Accepted 24 April 2026
Available online 28 April 2026

and degradation phenomena within the cell occur in the anode, cathode, and electrolyte at different rates, depending on the used materials and operation conditions. The underlying processes – including electrolyte decomposition, loss of active material (LAM), loss of lithium inventory (LLI), build-up of solid-electrolyte-interphases (SEI), and structural changes in the electrodes – collectively contribute to capacity fade and impedance increase over time, effectively decreasing the battery's energy capacity and power [1]. In particular Si-based anodes, attractive since they offer significantly increased specific cell capacities, suffer from unstable SEIs and a rapid consumption of active Li (LLI effect) in the consecutive reformation of the SEI after every cell cycle [2]. In addition, Si-based anodes present some challenges regarding calendar aging as well. A detailed discussion about the degradation mechanisms taking place on Si-based anodes is presented in Ref. [3]. The main results indicate that the ongoing SEI evolution suggests long-term electrolyte reactivity. This effect may exert a significant influence on cell impedance. Moreover, inefficient electrode utilization caused by electrolyte consumption is recognized as a primary factor limiting calendar life.

Conversely, the SoC represents the current charge level of the battery relative to its present maximum capacity at any point during lifetime; a dynamic parameter that changes with battery usage and is often connected to and determined by the cell's open circuit voltage (OCV), as a part of the electro-chemical cell analysis (EC). Precise SoC determination is crucial for effective energy management and for preventing detrimental conditions such as overcharging and deep discharging. Cathode and anode both have their individual SoC, depending on their SoH. This is usually investigated through half-cell potential analysis, since it cannot be distinguished by a full-cell voltage measurement alone.

Despite considerable advancements in battery technology and management systems, accurately assessing SoH and SoC remains a significant challenge due to the numerous and localised underlying effects. Traditional methods primarily rely on indirect measurements and empirical models, which are often fitted to application scenarios. Approaches combining traditional methods with novel characterization techniques in laboratory environments, e.g., imaging and elemental analysis, revealed potentially interesting aspects in Li-gradient detection [4], which can contribute to understanding operational and aging behaviour of batteries. This example highlights the shortcomings of traditional methods in capturing intricate electrochemical reactions, spatial cell inhomogeneities, and structural evolutions within the battery [5] and, at the same time, underscores the need for innovative diagnostic tools capable of revealing the underlying effects of battery degradation and charge dynamics [6].

In this context, MeV ion beam analysis (IBA) presents a groundbreaking approach to investigating the internal mechanisms of Li-ion batteries. Typically, Li is the key element for the processes in Li-batteries [7] and IBA is one of the few methods enabling its direct and spatial quantification. Leveraging the penetrating power of MeV ions, this technique enables the non-destructive tomographic probing of battery components, offering unprecedented insights into the spatial distribution of chemical elements, in particular Li. This enables investigating the loss of lithium inventory (LLI), loss of active material (LAM), SEI formation, and the kinetics of lithium intercalation and deintercalation processes. By providing a detailed tomographic analysis in particular of the Li concentrations and thus representing an alternative way for SoH and SoC determination, IBA holds the potential to unravel the complex interplay between material properties and battery behaviour. Finally, the atomistic understanding of the battery status provided by IBA on temporal and spatial scales enables developing, testing, and validating models to link SoC, SoH, and the battery operating conditions by providing data points required for model validation [8], [9].

It is known that in Si-containing anodes, massive volume changes can lead to SEI cracking as well as particle cracking, both revealing new particle surfaces on which continued SEI re-formation and thus LLI occurs. Particle cracking can be mitigated by utilizing nano-sized Si particles. However, this increases the surface per volume and thus again increases the surface area for SEI re-formation. Furthermore, the SEI in Si-anodes contains different components than in graphite anodes, since Si represents an additional element with more possible compositions. Besides Li_2CO_3 and LiF, Si anode SEIs contain Li_xSiO_y compounds [10], which potentially feature a lower ionic conductivity than the SEI components of graphite-based cells [11], [12]. Lower SEI conductivity and higher SEI thickness combine to a critical decrease of the ionic conductivity and inactivation of Li happening significantly faster in Si-based anodes compared to graphite-based anodes, reducing their cycle life. The Li inactivation additionally accelerates the anode ageing due to an increase in anode and a decrease in cathode potential in the order of 150 mV after ~200 cycles, which adds additional stress to the anode [13], [14].

To investigate the impact of Si in anodes and determine underlying mechanisms of cycling degradation on the electrode level, a combination of advanced micro-ion-beam analysis with AI-based data analysis is employed here for the first time. Using this approach, the quantification of Li and other elements relevant for SEI formation on the anode and composition of the cathode can be assessed both laterally and as function of depth, indicating if the effects are evenly distributed throughout the electrodes. Using the quantification capabilities of IBA, the Li-inventory can be accurately determined for various steps in the cell history and as function of cycling, allowing insights into the LLI and LAM mechanisms, including inactivation of Li, transition metal leaching, and anode-cathode cross-talk. Finally, the spatially resolved data are used to validate modelling data, e.g. continuum models predicting lithiation degrees and over-potentials. This approach provides a powerful tool for existing and new battery chemistries, like NCA + Si/G, enabling a mechanistic understanding based performance improvement.

2. Methods

2.1. Ion beam analysis

The sample is analysed using the Aachen Ion Beams BeamScience end-station [15]. This instrument is supported by a 1.7 MV tandem accelerator fed by a multi-cusp negative ion source. The accelerator provides 2.98 ± 0.02 MeV protons at 7 nA current in a focussed 50 μm diameter spot on the sample. A triple quadrupole magnet with 9 mm bore and 100 mm length is used for focussing. It is equipped with a 300 μm and a 1500 μm Si-PIN detector at 150° reaction angle, a KETEK SDD with 130 eV full-width-half-maximum (FWHM) and 125 μm Be window at 112.5°, and a HPGe detector at 0°. The data acquisition is synchronised to 5-10 ms differences in spectral acquisition time through the data acquisition software. The ion current is measured using a +300 V bias applied to the insulated sample through a tri-axial wire connected to a Keithley 6485 A m with an effective resolution of 10 pA. The fixed-beam geometry applied here results in a high freedom of choice for the manipulator. The high-resolution (10 nm) manipulator applied here allows for scan areas of up to 49 × 49 mm^2. The device's control software synchronises the data acquisition of all detectors and saves spectra and metadata.

For measurement evaluation, the $^7Li(p, \alpha)^4He$ reaction and (p,p_x) reactions for ^6Li and ^7Li with cross-sections from Ref. [16] for Li and ^{19}F $(p, \alpha_0)^{16}O$ for F are used. All other elements were evaluated by SigmaCalc (Li, O, C, F, P, Si) or Rutherford cross-sections in the same software. SimNRA 7.04 with SRIM2013 stopping data [17] are chosen for spectrum modeling and fitting. The options fast pile-up, multiple-scattering, and no dual-scattering are selected. The evaluation is based on elemental depth profiles described by an error function. The fitting is executed in two steps. First, a neural network is trained on a manually evaluated anode or cathode reference spectrum which is varied automatically to extend the parameter range. This neural network provides an educated guess for a fine-fitting using a differential evolution algorithm [18]. This way less iterations for the fine-fitting are required,

while the mathematical rigor of a classical fitting algorithm is preserved. Besides Rutherford-Backscattering Spectrometry (RBS) and Nuclear-Reaction-Analysis (NRA) also Particle-Induced-X-ray-Emission (PIXE) spectra are acquired on a KETEK SDD with ≈130 eV FWHM energy resolution. GUPIX3 [19] is used for PIXE spectrum evaluation. GUPIX fits the data using the "iterated matrix solution" with up to 5000 iterations. The processing of 10,000 individual data points each having four spectra plus metadata runs on a 64 core workstation PC within about 2 days.

2.2. Ion beam analysis of batteries

An earlier study regarding the SoC demonstrated the importance of IBA accuracy, since only a small fraction of the total Li is mobile [20]. This requires high counting statistics in the IBA spectra and accurate data interpretation through fitting of a physics model. Each IBA point is integrated to 2 μC = $1.3*10^{11}$ Particle*Sr. This results in about $3*10^6$ total counts per spectrum and about 20,000 counts in the ^{7}Li(p, α)^{4}He reaction which is used for Li quantification. The related statistical uncertainty in the presented elemental concentration accounts to 0.7%, which has to be added to a 2% statistical uncertainty introduced by the data fitting. The data fitting quality is assured by comparing the 2160 cathode and anode data points. A strong inhomogeneity beyond a factor 2 in the Li content cannot be expected for single isolated points. No data beyond this limit is observed, supporting the assumption of a stable fitting procedure. Consequently, the relative uncertainty in the Li concentration is in the order of 2%. The systematic uncertainty in the elemental concentration is 5% contributed mainly by the ^{7}Li(p, α)^{4}He cross-section uncertainty [16]. Statistical uncertainties influence the homogeneity of the results, while statistical and systematic uncertainties apply to the quantification of SoH and SoC.

The IBA sensitive range in the anode and cathode materials depends on their porosity and elemental composition and lies in the order of 40 μm. A clear indication for probing the whole layer thickness is a visible signal of the Cu (Anode) or Al (cathode) substrate. This is seen in all anode layer data points, but in no cathode layer data point. The cathode probing range can be derived from SimNRA through testing of the signal variation for different layer thicknesses. A maximum range of $2.4*10^{24}$ atoms/m^2 is found, which corresponds to 60% of the cathode layer thickness according to the mass loading from the cell manufacturing. Therefore, the Li amount found by IBA in the cathode must be multiplied with a factor of 1.67 to scale to the full cathode thickness.

2.3. Cell preparation

For the experiments, a single cell containing a Si/Graphite anode with 69.7 wt% Si, 19.9 wt% graphite, 8.2 wt% LiPAA, and 0.2 wt% CMC is used. The silicon (CLM 00001) was provided by Wacker Chemie AG. The graphite is electrochemically inactive by design [21]. The cathode is a $LiNi_{0.8}Co_{0.15}Al_{0.05}O_{1.985}(BO_3)_{0.01}$ (NCA) containing 2 wt% PVdF and 2 wt% carbon black. The NCA was provided by BASF. The Si/NCA cells were built at *iwb* (Institute for Machine Tools and Industrial Management) at the Technical University of Munich, and wetted with the electrolyte 1M $LiPF_6$ FEC/DEC (1:4 by vol.). A total of 29.1 g_{NCA} and 5.005 g_{Si} were used for cell coating. Only 30% of the anode capacity is utilized to avoid excessive volume changes [21]. Therefore, the specific capacity of the anode comprises 1200 mAh/g_{Si}. The final cell design provides a specific capacity of 185 mAh/g of NCA. The anode foils have a coated area of 111.8 mm × 81.80 mm and the cathode foils a slightly smaller area of 111.0 mm × 80.00 mm. It consists of a stack of 11 anode and 10 cathode layers contained in a pouch bag. One anode layer is on the outside of the cell stack with no opposite cathode layer. This anode layer will be neglected. The double-coated anode thickness is on average 150 μm and the cathode thickness 165 μm. This includes a 15 μm thick copper (anode) or aluminium (cathode) foil and two coating layers. Each layer features a single current tab of about 10 mm width in the centre of the 80 mm.

2.4. Cell cycling

After assembly at *iwb*, the cell underwent cyclic aging with intermediate diagnosis tests to determine the SoH by tracking the cell capacity and resistance. Aging cycles were conducted at C/2 CC C/20 CV charge and C/2 discharge. Diagnosis tests consist of two cycles at C/10 CC C/50 CV and 1 h of rest after charge and discharge, each. In total, 376 cycles between 4.2 V and 2.8 V were applied to the cell. Figs. 2 and 3 show the voltage profile over capacity as well as the evolution of remaining capacity and internal resistance. At begin of life, the cell can provide a capacity of 185 mAh/g_{NCA}, which translates to a variation of X in $Li_XNi_{0.8}Co_{0.15}Al_{0.05}O_{1.985}(BO_3)_{0.01}$ between 0.14 and 0.8, corresponding to 4.45 at.% Li at SoC = 100% and 21.05 at.% Li at SoC = 100% [22]. After 376 cycles, the cell was stored for approx. 2 years at room temperature and 50% SoC. Before disassembly, it was discharged to 0% SoC and stored for 1 additional month. Table 1 below summarizes the history of the cell.

The disassembly of the cell was performed in an argon-filled glovebox. From the stack of anodes and cathodes, the middle as well as the top anode and cathode foils were extracted (four foils in total from a single battery). Each foil was then segmented into a matrix of 3 × 3 samples of about 36 × 26 mm^2, which were then used for the ion beam analysis.

2.5. Study of preparation effects

Effect of sample preparation after extraction of the foils from the pouch bag potentially influence the IBA result. Furthermore, the background of the immobile Li concentration related to compounds used in cell manufacturing and preparation (Li-salt from electrolyte and Li-based binder) is highly relevant for SoH and SoC determination. Therefore, anode samples in pristine (no electrolyte applied), wetted pristine, formed (after 1st cycle), and washed formed (after 1st cycle and Li-salt removed) state are investigated. Table 2 shows the results.

The electrolyte and its conductive salt apparently contribute only a negligible amount of Li to the overall content. This background signal of Li is related to the initial SEI and possible electrolyte salt residue, which are subtracted from the SoH and SoC considerations in the following. The pristine anode contains 1.88 at. % Li, which is attributed to the LiPAA binder. This fraction of Li is considered inactive. The pristine cathode contains 21.94 at.% Li considering all elements, but the nominally expected 25.4 at.% Li when considering only NCA. The formation process removes 2.34 ± 0.31 at. % Li from the cathode and adds 4.88 ± 0.12 at.% to the anode (electrolyte wetted vs. SEI formed not washed). Taking into account the different atomic thicknesses (factor 1.8) and areas (factor 0.97) of anode and cathode we obtain an almost match corresponding to the required conservation of the Li atoms.

Washing of the anode reduces its F and P content strongly, but O and Li remain mostly constant and on the level of the wetted case. Among the

Table 1
History of the cell since begin of life until disassembly for IBA. Aging cycles consist of 1C CC C/20 CV charge-discharge cycling. Diagnosis cycles are conducted at C/10 instead of 1C. Storage took place at room temperature.

REPETITIONS	LOAD PROFILE	ACCUMULATED CYCLES
1	Formation & Stabilization procedure	10
1	(10x aging cycles + 2x diagn. cycles)	22
2	(20x aging cycles + 2x diagn. cycles)	66
5	(40x aging cycles + 2x diagn. cycles)	276
4	(20x aging cycles + 2x diagn. cycles)	364
1	(10x aging cycles + 2x diagn. cycles)	376
1	1 year storage at 50% SoC	376
1	Discharge to 0% SoC, 1 month storage, disassembly & sample preparation for IBA	376

Table 2
Li concentrations in the investigated battery type before operation and after certain preparation steps. Electrolyte wetting clearly increases the Li concentration. The SEI formation moves Li from the cathode to the anode. Washing out the electrolyte + $LiPF_6$ removes 0.69 at.% Li. Values are determined from 20 IBA points per sample filtered using a fitting quality parameter resulting in uncertainties of 2%. The atomic percentage relates to all elements including binder, electrolyte, and carbon.

Step	Li atom % in anode	Li atom % in cathode
Pristine	1.88	21.94
Electrolyte wetted pristine	5.97	22.74
SEI formed, dried, not washed	10.85	20.40
SEI formed, dried, washed	10.16	19.71

several typically assumed SEI contributions $C_4H_4Li_2O_6$ [23], Li_2CO_3, LiF, LiP_xO_y, and Li_xSiO_y [10] this indicates a negligible contribution of LiF in this case.

2.6. SoC and SoH determination

The SoC = 100% is defined as the electrochemical state corresponding to a cell voltage of 4.2 V. In order to increase the cycle life, this does not correspond to a full de-lithiation of the cathode or a full lithiation of the anode. The cycle life drops significantly when exceeding the nominal lithiation degrees. Table 3 discusses a few exemplary cases based on literature values for the Li concentration to highlight the sensitivity of IBA for different cell states.

The local electrode SoC can be derived from the Li atomic concentration through a linear scaling between maximum and minimum Li percentage in the active materials. For this exemplary calculation it is assumed that for NCA at SoH = 100%, X in $Li_XNi_{0.8}Co_{0.15}Al_{0.05}O_2$ is between 0.80 and 0.14 for SoC = 0% and 100%, respectively. For $X = 1$ a maximum value of 25 at.% Li in the as-prepared state of NCA is reached (Li has 1 of 4 stoichiometric points). For Si at SoH = 100%, limits for X in $Li_XSi_{4/15}$ between 0.04 and 0.30 for SoC = 0% and 100% are assumed. For $X = 1$ a theoretical maximum value of 78.95 at.% Li in the Si (neglecting binder, graphite …) can be reached.

This Li relates to the NCA in the cathode and to the Si in the anode. Other components such as binders, electrolyte, impurities, and so on have to be separated mathematically. If the SoH of an electrode reduces, its minimum Li concentration increases due to the added immobile Li, while the maximum remains constant due to the conservation of the total Li amount. If only one electrode dominates the aging, as depicted in this work, the maximum of the other electrode's Li concentration is reduced since the required Li cannot be extracted from the first electrode (conservation of total Li). For the investigated cell type, the anode aging dominates. The table assumes that the aging does not influence the electrode half-cell potentials, which is probably not true as the voltage shifts in Fig. 2 and the non-linear capacity fading in Fig. 1 indicate. The last row "Discharged, anode aged" depicts the case assumed to represent the investigated sample (see Fig. 1). With decreasing SoH in the case of anode aging, both Li concentrations in the discharged state SoC = 0% approach each other. In contrast, in the cathode aged case, the Li concentrations at SoC = 100% approach each other. This enables separating these two aging mechanisms through IBA. If a single electrode dominates the aging analysing one SoC is sufficient, while in a mixed aging both SoC = 0 and SoC = 100% have to be compared.

Table 3
Examples of battery cell states investigated by IBA. We assume a liquid electrolyte NCA cathode and a 1:1 atomic fraction Si/Graphite anode. Si is assumed to bind up to 1 Li atom per Si atom and graphite 1 Li per 6 carbon atoms. Contributions by electrolytes and other cell components are not considered. Typically, conductive salts contribute a few % of the total material and represent a certain inactive amount of Li even in a fresh cell. The cell is assumed to feature identical capacities for anode and cathode.

Status cell	Status ageing	SoC [%]	SoH [%]	Anode Li [at.%]	Cathode Li [at.%]
Charged	fresh	100	100	52.94	4.46
Discharged	fresh	0	100	3.61	21.05
Charged	only cathode aged	100	70	38.14	9.44
Discharged	only cathode aged	0	70	3.61	21.05
Charged	only anode aged	100	70	52.94	4.46
Discharged	only anode aged	0	70	18.41	16.07

3. Results and discussion

3.1. Investigated battery cell

The investigated 5.38 Ah battery consists of 20 cathode-anode layer pairs with NCA ($LiNi_{0.8}Co_{0.15}Al_{0.05}O_{1.985}(BO_3)_{0.01}$) cathode, Si/Graphite anode, and a liquid electrolyte. The details of cell manufacturing, composition, and cycling can be found in the methods section. During its lifetime, the stack is sealed in a pouch bag, see Fig. 1.

The cell is cycled 340 times from 2.8 to 4.2 V at 25 °C, then stored at SoC = 50% at 25 °C for ~12 months, before finally being discharged and disassembled at 2.8 V (SoC = 0) to be analysed via IBA. Fig. 2 shows two exemplary charge/discharge curves during battery life to indicate its strong deterioration with decreasing SoH.

Fig. 3 depicts the continuous reduction of the SoH measured by its Ah capacity. 30.7% = 1.65 Ah of the initial capacity is lost after 340 cycles compared to the discharge capacity of the first cycle. The charging cycles show a decrease of 1.74 Ah in capacity compared to the first charging cycle after formation. At the same time, the internal resistance measured via direct current (DC) pulses increased by a factor of 2.3. These changes are non-linear and the loss of SoH accelerates with cycle count.

A preparatory study investigated the composition in a pristine cell. Four preparation stages are investigated to reveal the amounts of passive Li originating from the cell preparation and enable separation from the aging related changes. Further details are given in the method section, see Table 2.

3.2. Tomographic analysis

In the preparatory study discussed in the methods section (SoH = 100%), we find at SoC = 0 a 10.16 at.% Li concentration in the anode

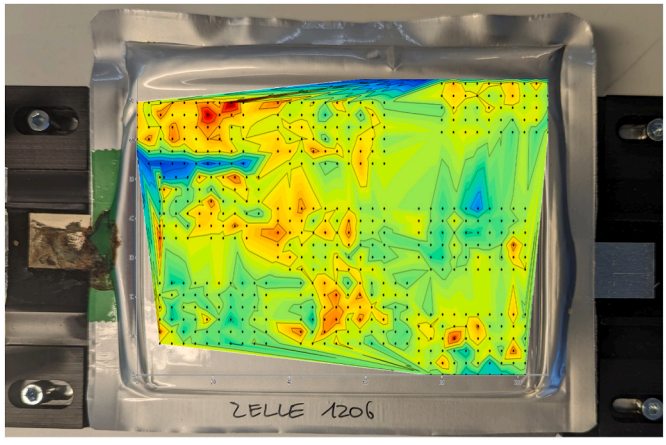

Fig. 1. Overlay of linear interpolation map of Li/Si ratio and pouched cell photo. The black dots represent individual analysis points. The cell terminals are visible on the left and right side. The electrolyte is injected from the top-left edge.

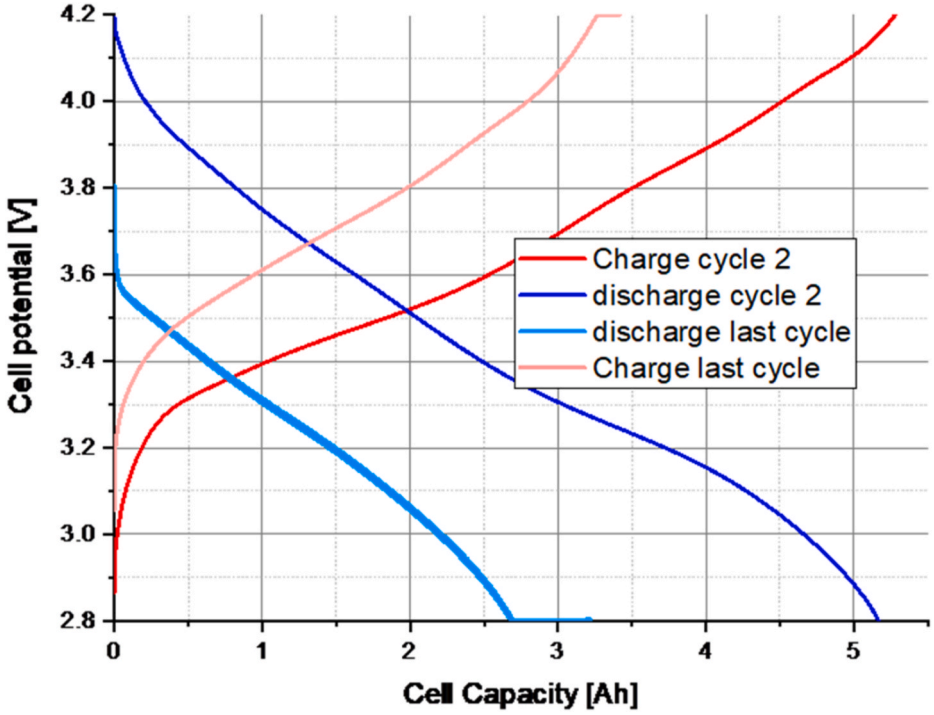

Fig. 2. Charge-discharge curves of the second and the last cycles. Cycle 1 represents the formation, cycle 2 the first representative cycle, and the last discharge already shows a significantly reduced capacity. Operating temperature 25 °C, dis-/charge rate 0.1C = 0.3 mA/cm^2.

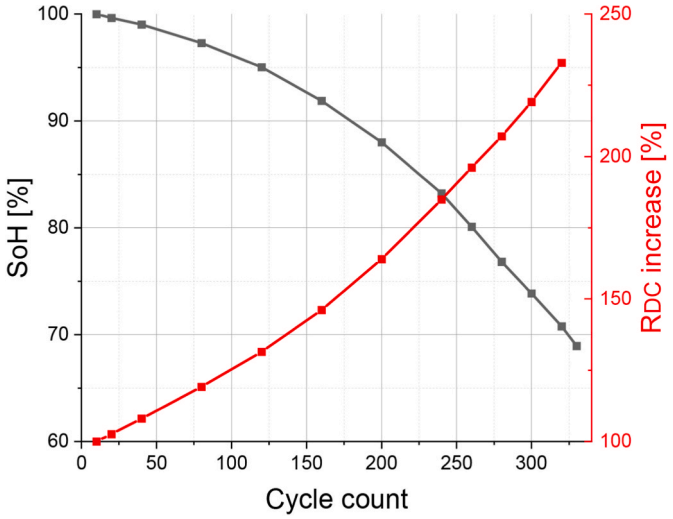

Fig. 3. Cell SoH and DC resistance (R_{DC}) at 0% SoC vs. number of cycles. The initial capacity of 5.38 Ah reduces by 1.65 Ah (30.7%) to 3.73 Ah after 340 cycles. Typically, 70% SoH is considered the end-of-life due to the accelerated capacity decrease thereafter. The inner DC resistance increases from 22 mΩ to 51 mΩ (factor 2.3). The resistance increase is similar for SoC = 25%, 50%, and 75%. Both slopes match with $R^2 \geq 0.9995$ to quadratic polynomials.

related to binder + SEI + @2.8 V intercalated Li. Literature modelling results show $\chi_{0,Si}$ = 4.0% [22], which equals 6.55 at.% mobile Li (calculated from the maximum Li atom loading of 3.75 Li/Si). The binder adds 1.88 at% Li and the electrolyte introduction adds another 5.97-1.88 = 4.09 at.% Li to the total Li-inventory of the anode. The formation transfers another 10.85-5.97 = 4.88 at. % Li from the cathode to the anode. Therefore, our experimental $\chi_{0,Si} \leq 3\%$. We can only state an upper limit of $\chi_{0,Si}$ since this Li consists of intercalated plus SEI-bound Li.

Using IBA, we measure a total of 19.71 ± 0.5 at.% Li in the cathode, corresponding to 22.7 ± 0.5 at. % Li in the NCA active material. This corresponds to a $\chi_{0,NCA}$ = 0.88 ± 0.02, which is close to the probably underestimated theoretical $\chi_{0,NCA}$ = 0.80 from Ref. [22]. The observed slight deviations between previous modelling results and the IBA results can thus be used for a refinement of the used models.

For the analysis of the cycled cell, two anode (A) and two cathode (K) foils are removed and dried. Two foils are extracted from the middle (KM and AM) and the top (KT and AT) of the cell stack. The IBA imaging shows lateral variations of the layer composition and the cathode thickness on these foils in the % range, see Fig. 4. The figure shows an average Ni concentration of 49 ± 3 wt% in agreement with the nominal value of 47 wt%. The first mm on the outer edge of the cathode layers shows somewhat lower Li concentrations, probably due to the anode layers being 1 mm larger in all dimensions than the cathode layers. A temperature sensor is placed in the cell centre during the cycling experiments. This additional pressure introduces a slight additional inhomogeneity in the order of 2%.

IBA provides atomic concentrations and amounts of atoms per area. Aligning this information with the common battery parameters of charges, voltages, and stoichiometries requires a different approach of thinking. Charge transfer is connected to the decrease and increase of the Li concentration in both electrodes since every elemental charge corresponds to a single Li ion exchanged between anode and cathode. Since not all Li ions are electrochemically active, not every Li atom detected by IBA represents a transferable charge. Voltages and currents (e.g. the open-circuit-voltage OCV or the SoC) are related only to the active fraction of the measured Li concentration, therefore small changes in the Li concentration can induce strong changes in the voltages. The difference between moved charges (=active Li) and IBA detected Li atoms (active + inactive Li) yields information on SoC and SoH.

In stoichiometries, typically *X* denotes the amount of an element changing in a process, while in a concentration, which is provided by IBA, the reduction of one element will increase the concentrations of the remainder of the elements. The cell is analysed on 2160 points, each containing a full set of elemental spectra as a function of depth, enabling

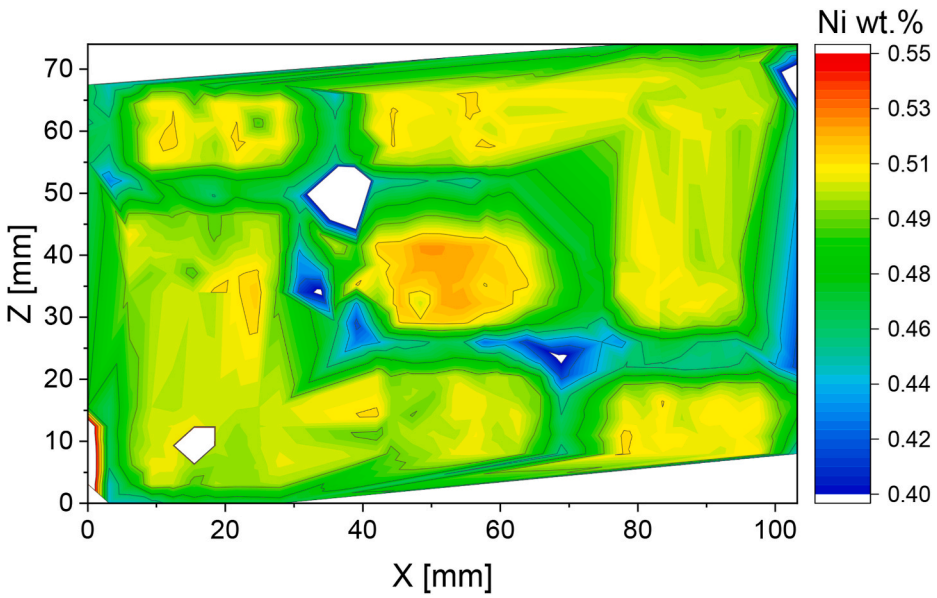

Fig. 4. Plot of the depth-averaged Ni areal-concentration in weight% of the KM sample. The figure shows ±6% inhomogeneities in the lateral distribution of the cathode coating thickness represented by the Ni content. The current tap is on the centre of the left edge. In the centre a temperature sensor was mounted, inducing additional pressure onto the material. Removed outliers are shown as holes/white.

the quantitative determination of the elemental composition in 3D. However, analysing such a large amount of data consistently is only possible using AI-based algorithms, developed previously by some of the authors [18], [24]. Using these advanced analysis capabilities enables the compilation of 3D elemental maps of the electrodes by fitting depth profiles for each of the 2160 data points with 20 intervals each for the 7-8 elements of interest for the cathode and anode (out of Li, C, O, F, P, Al, Si, Co, Ni), resulting in ~345,000 concentration data points determined in this study. In order to reduce the data complexity, the important elements and their concentrations or ratios will be presented in this section. The complete dataset is available in the repository [25].

The measured 3D concentration map for Li for a single electrode sheet (AM) is shown in Fig. 5. This depth analysis reveals largely different elemental concentrations in the outer surface compared to the nominal and bulk values. This surface layer is typical for battery materials shortly exposed to air or stored over long durations, since Li_2CO_3

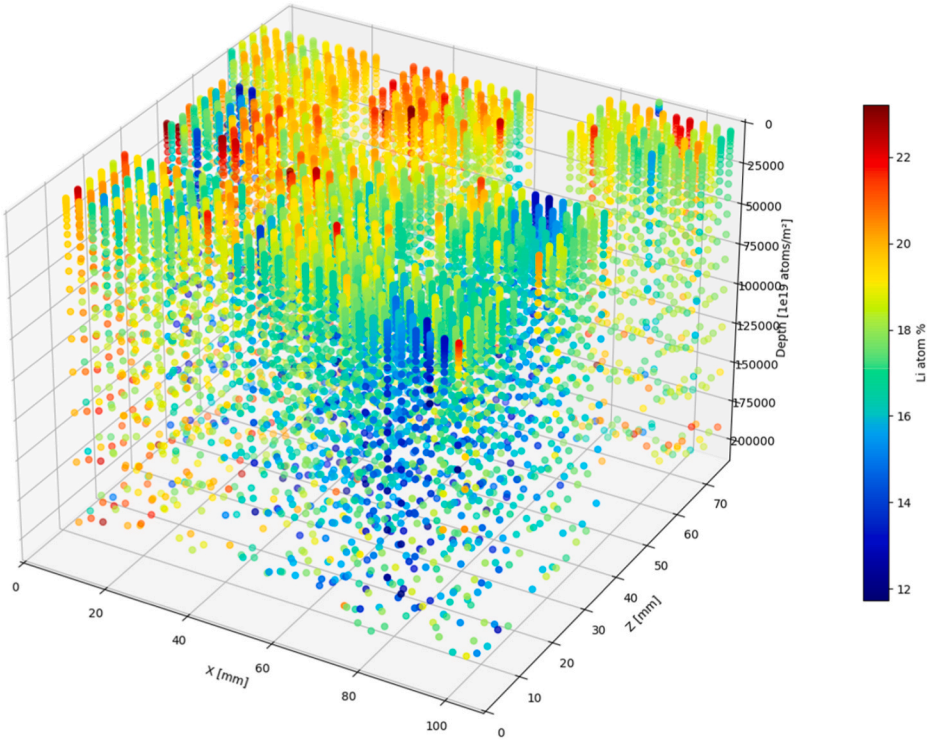

Fig. 5. Tomography image of the Li concentration in sample AM with 11,000 points. On average, an atomic concentration of 17.8 atom % Li is found. A surface effect due to the short contact with air is visible with constant bulk concentrations below this. The point density reduces towards the depth due to the reducing depth resolution in deeper parts.

and LiOH form on the surface together with ambient air, which typically lowers the Si- and raises the Li concentration. The effect cannot be attributed to thick solid-electrolyte interface layers (SEI), since this would alter the concentrations in the layer volume homogeneously, considering the IBA spatial resolution and range are >10x larger than the grain size in this case. Therefore, this layer is neglected for our considerations.

3.3. State-of-charge/mobile Li inventory

The cell is analysed after 340 cycles and in the SoC = 0 state where effectively no mobile Li should be left in the anode. From the last discharge cycle the capacity is known to be 3.71 Ah, representing the amount of mobile Li in the cell, which should be completely in the cathode. The total amount of Li is measured for each electrode individually by IBA. The total amount of Li detected by IBA in all cathodes and anodes by extrapolating to the area of 111 × 80 mm^2 and the design with 20 cathode and 20 effective anode layers (1 dead anode layer due to production) yields a global sum of $3.6*10^{22}$ Li atoms in the cathode and $8.04*10^{22}$ Li atoms in the anode. This translates to 16.0 at.% Li in the cathode, compared to the pristine state a loss of more than 4% points compared to the nominal Li concentration of 20.4%. In contrast, the anode showed a total Li concentration of 17.4 at. % Li, a gain of 7.2 % points during cycling compared to the initial formation. The cathode lithiation degree corresponds to a half-cell SoC = 20%, in contrast to the full-cell SoC = 0%. With $6.25*10^{18}$ ions/Coulomb and 3600 C per Ah we obtain a remaining cathode capacity until SoC = 100% (=4.45 at.% Li) of 3.42 ± 0.2 Ah, which compares well to the remaining capacity of 3.7 Ah. The total detected cathode Li equals 5.38 Ah. Compared to the initial discharging capacity of 5.38 Ah this equals a capacity loss of 1.92 ± 0.2 Ah derived from IBA. The anode analysis shows a content of 8.04 ± $0.4*10^{22}$ Li atoms equal to 3.57 Ah of immobile Li. In comparison to the as-prepared amount of Li in the anode of 2.17 Ah seen in the preparation study we see an immobilization of 1.4 ± 0.4 Ah in the anode. The results compare well to the initial 5.38 Ah, the remaining 3.71 Ah capacity, and the 1.65 Ah of capacity fading from EC considering the uncertainties of charging and discharging capacity measured by EC and the possible discrepancies between the cell used for the preparation study and the cell used for the capacity fading analysis.

3.4. State-of-health determination via ion-beam analysis

Similar to the SoC, the SoH is typically determined by EC through the loss of capacity and an increase in resistivity in comparison to the fresh state of the cell. After the applied 340 cycles, the cell has a global SoH of 69% regarding the capacity, while the internal resistance increased by a factor of 2.3. IBA can only assess the SoH in terms of loss of capacity. The SoH is determined from the decrease in mobile Li bound in the anode. At SoC = 0 the amount of Li determined in the pristine state, see the methods section, has to be subtracted. We see a binding of 3.57 ± 0.2 Ah of Li in the anode foils compared to 2.17 ± 0.2 Ah in the pristine state (of a different cell of the same type). Therefore, 1.4 ± 0.3 Ah of capacity is additionally immobilized in the anode, which agrees with the electrochemical measurement of 1.65 Ah.

We have numerous possible compounds (Li_4SiO_4, Li_2SiO_3, $LiPO_3$, Li_3PO_4, $Li_4P_2O_7$, Li_2CO_3, LiF …) which could contribute to the SEI. Silicate formation is a potential candidate for the faster SEI formation and capacity fading of Si-based anodes [23], making it interesting to quantify its amount. IBA can only access the elemental composition, not the chemical situation, but by forming an equation system of the elements and possible compounds, the chemical situation can be derived. LiF can be quantified from the elemental composition, assuming that all $LiPF_6$ salt is removed by the washing step prior to the IBA analysis, the remaining F is present as LiF. A similar assumption is possible for the three lithium phosphates, but the range of 1-3 Li per P atom does not allow separating phosphate mixtures. The lithium silicates are compounds which are present in parallel to the still active part of the Si. Since we know at SoC = 0 there is no active Li, all present Li has to be attributed to SEI compounds.

Table 4 and.

Table 5 show the measured anode and cathode compositions. While the cathode foil compositions are almost identical, the two anode sheets have a significant difference, especially in their F content, which cannot be explained at this point. P should not be present in the anode since the electrolyte is removed before analysis. Therefore, the detected P is considered to be bound in phosphates with up to 3 Li per P (Li/P ranging from 2 to 3) equal up to 5.4% points of Li bound in phosphates. LiF binds 1 Li per F. Li can be present as Li metal, but this is electrochemically unfavourable and therefore neglected. The O could be bound in silicates, phosphates and SiO_x or LiC_xO_y, making it an ambiguous indicator for silicate formation. From these values we can derive the Li potentially bound in silicates and the amount of silicates, which represent an additional path for Li immobilization specific to Si anodes. In the AT foil the silicate value remains compatible with zero, while in the AM foil silicates are required but their contribution to the capacity fading remains below 1/3. In conclusion, silicate formation cannot explain the accelerated capacity fading of Si-anodes.

The observed differences in anode composition can introduce an additional uncertainty in our IBA-based analysis, since it remains unclear if the average of the four analysed foils holds true for the average of all foils in the cell. The close match of the Li values indicates that the additional uncertainty remains small.

Comparing our SEI composition results to the literature shows a general agreement with our LiF dominated SEI observation. Since IBA is a new approach in this field with a unique strength for light element quantification but a limited separation of SEI and the anode bulk, its results naturally differ from established analysis approaches with different analytical properties. Several studies analysed the SEI composition in Si-anodes using electron microscopy, x-ray photoelectron spectroscopy, and others. The impact of the electrolyte on the SEI composition is significant, since the F content can differ by one order of magnitude already between LiPF6-FEC and LiPF6-EC [26]. An F content of 32.8% and an LiF dominated SEI with a small Li_xSiO_y contribution was found in Ref. [26]. A similar result with a LiF dominated SEI with contributions of polyene is found in Refs. [27], [28].

4. Conclusions

The electrodes of a close-to-industrial 5.38 Ah Li-ion battery using NCA + Si/G chemistry is analysed post-mortem using IBA. Using micro-ion-beam measurements and AI-based analysis, extremely large datasets are compiled providing 3D tomography information on the elemental composition. This is used as an independent measure of the state-of-health and state-of-charge of the cell, verifying the 0D data from electrochemical analysis (EC) and literature data. The combined EC + IBA analysis provides a deeper insight into the aging mechanisms responsible for the capacity fading of the used Si-anodes.

Minor lateral inhomogeneities in the coating thicknesses are observed in some cases. The individual electrode foils differ by up to 6% in their Li content, in particular in the anode. This inhomogeneity is most likely connected to inhomogeneous SoH between different anode foils, since ageing and thus loss of SoH mainly occurs on the anode-side for the investigated cell. Along the depth axis of the individual electrode foils no inhomogeneities are detected, except for an analysis preparation related effect. These results correlate well with the results of [29], where long voltage hold measurements were performed on the same Si-based pouch cells. The authors found long-lasting transient phases on the leakage current results. The main causes discussed are relaxation effects due to Si-hysteresis and SoC inhomogeneities over the surface of the electrodes, which do not allow the leakage current to reach a stable value.

We see SEI formation and the corresponding Li entrapment are

Table 4
Data comparison of the measured anode compositions obtained by forming the mean of all values obtained for the respective sample. The Li_xSiO_y fraction is calculated by assuming every F atom is bound in LiF and every P atom is bound in $Li_4P_2O_7$, then subtracting Li in LiF and $Li_4P_2O_7$ bindings from the Li atom%. Due to the correlation between the concentration values we approximate the IBA uncertainties to ±0.5 percent points. Summing up these uncertainties over the 6 observed elements makes the −1.2% Li_xSiO_y compatible with zero. The P/F = 6 ratio of $LiPF_6$ is roughly in agreement to the data.

Sample	Li atom%	F atom%	P atom%	C atom%	O atom%	Si atom%	Li atom% in Li_xSiO_y
AM	17.8 ± 0.5%	8.5%	1.8%	31.5%	10.0%	30.4%	5.7 ± 3.0%
AT	17.3 ± 0.5%	14.3%	2.1%	28.9%	11.0%	26.3%	−1.2 ± 3.0%

Table 5
Data comparison of the measured cathode compositions obtained by forming the mean of all values obtained for the respective sample. The Li in NCA value relates Li only to Li+(Ni + Al + Co) + O. IBA uncertainties are in the range of ±0.5 percent points in the concentrations. The P and Al contents are below the detection limit and therefore set to 0.

Sample	Li atom %	F atom %	Ni + Co atom%	C atom %	O atom %	Li atom% in NCA part
KM	16.1%	4.0%	23.3%	14.6%	41.5%	18.9%
KT	15.9%	3.7%	23.2%	16.0%	41.1%	18.9%

responsible for both capacity fading and internal resistance increase. The immobilized Li is clearly found in the anode, the cathode did not undergo significant deterioration, as expected for NCA. The shift in mobile Li changes the lithiation limits of the anode and cathode which cannot reach the experimental pristine SoC = 0 lithiation state of $\chi_{0,NCA} = 0.88$, but only $\chi_{0,NCA} = 0.67$. This leads to a shift in the cathode potential of +130 mV and in the anode of −130 mV [13]. The resulting potential shift is in agreement with the literature [11]. Correspondingly, the shifts in the half-cell potential during cycling lie outside the range considered safe for reversible operation leading to an accelerated degradation of the cell with ongoing cycling. This fits to the observed non-linear capacity fading in the EC analysis shown in Fig. 3.

The results show a strong decay of the SoH related to the ~17 at.% of Li found in the anode. The observations of silicate formation contributing less than 32% of the SEI indicates only minor relevance of Li bound in silicates for the accelerated capacity fading of Si-anodes. This enables attributing the observed capacity fading of 31% to an immobilization of Li in the anode. The immobilization is shown to happen through SEI formation. Increased F and P concentrations found in the washed cell foils, originating from $LiPF_6$, support this assumption resulting in mainly LiF and lithium phosphate with only little Li_xSiO_y forming the SEI. The results suggest that the presence of Si increases the LiF formation rate possibly by exposing fresh surface due to the large volume change of Si upon cycling and subsequent SEI cracking or Si/silicates could act as a chemical accelerator/catalyser for the LiF, e.g. through HF scavenging in combination with the FEC in the electrolyte [30], [31] or through water impurities in the cell [3].

The data suggest that the lithium loss mechanism related to the SEI formation is mostly similar to graphite anodes but the formation process is accelerated, since lithium silicates are at best a minor SEI component. Therefore, the ansatz for suppressing the fast capacity fading of Si anodes requires electrolyte (salt and solvent) optimization similar to graphite anodes. The increased cell impedance can be indirectly derived from this SEI formation, since the SEI contains low Li conductivity components. A quantitative comparison with the factor 2.3 increase in the internal resistance is not possible at this stage.

For cell improvement, the following conclusions can be drawn from the presented results for the investigated cell type. The capacity fading can be delayed by increasing the amount of available Li, e.g., by a thicker cathode coating or a pre-lithiation of the anode. This would delay the electrode potential shifts with decreasing SoH, delaying the connected non-linear capacity fading. With decreasing SoH the cell capacity becomes limited by the mobile Li in the cathode. A 2.4 Ah = 480 mAh/g_{Si} ≈ 0.66 g Li pre-lithiation (derived from the Li bound in the anode during formation and the 340 cycles) of the anode would have completely suppressed the potential shift and the SEI formation related capacity fading effect in the aged battery. In Ref. [32] the maximum of the discharge capacity increase by pre-lithiation was found to be located between 360 and 1200 mAh/g_{Si}, in agreement with our result of 480 mAh/g_{Si}. Additionally this would increase the $\chi_{0,NCA}$ from 0.77 to 0.88 in the SoH = 100% state, increasing the initial capacity by 14% (8% in Ref. [32]). Literature demonstrated the positive effect of the pre-lithiation, but could not explain the discovered optimal value of about 600 mAh/g [32]. Additives could suppress the cell impedance increase by making the SEI more conductive. The SEI growth probably relates to the SEI cracking due to the large volume change of Si-anodes upon cycling, but silicates potentially also act as a chemical accelerator for the LiF formation, therefore influencing the LiF formation cycle through additives or less available F could potentially reduce the SEI formation rate with cycling. Going away from fluorinated components such as $LiPF_6$ could close the LiF formation route, further reducing the LiF dominated SEI formation.

CRediT authorship contribution statement

S. Möller: Conceptualization, Data curation, Formal analysis, Investigation, Methodology, Software, Validation, Visualization, Writing – original draft, Writing – review & editing. **Axel Durdel:** Formal analysis, Investigation, Methodology, Visualization, Writing – review & editing. **Luiza Streck:** Formal analysis, Investigation, Methodology, Visualization, Writing – review & editing. **K.F. Muzakka:** Formal analysis, Software, Visualization. **M. Finsterbusch:** Conceptualization, Funding acquisition, Writing – review & editing.

Declaration of competing interest

The authors declare that they have no known competing financial interests or personal relationships that could have appeared to influence the work reported in this paper.

Acknowledgments

This research was funded by the Federal Ministry of Education and Research (BMBF) within the project "For-Analytik" (grant number 13XP0445). The battery and its materials analysed here are the result of the ExZellTUM III research project (grant number: 03XP0255), which was funded by the German Federal Ministry of Education and Research (BMBF).

Data availability

All data generated or analysed during this study are included in its supplementary information files or available under https://zenodo.org/records/14096284 [25].

References

[1] C.R. Birkl, M.R. Roberts, E. McTurk, P.G. Bruce, D.A. Howey, Degradation diagnostics for lithium ion cells, J. Power Sources 341 (Feb. 2017) 373–386, https://doi.org/10.1016/j.jpowsour.2016.12.011.

[2] L. Sun, Y. Liu, R. Shao, J. Wu, R. Jiang, Z. Jin, Recent progress and future perspective on practical silicon anode-based lithium ion batteries, Energy Storage Mater. 46 (Apr. 2022) 482–502, https://doi.org/10.1016/j.ensm.2022.01.042.
[3] J.D. McBrayer, et al., Calendar aging of silicon-containing batteries, Nat. Energy 6 (9) (Sep. 2021) 866–872, https://doi.org/10.1038/s41560-021-00883-w.
[4] B.-G. Chae, S.Y. Park, J.H. Song, E. Lee, W.S. Jeon, Evolution and expansion of Li concentration gradient during charge–discharge cycling, Nat. Commun. 12 (1) (Jun. 2021) 3814, https://doi.org/10.1038/s41467-021-24120-w.
[5] H. Tian, P. Qin, K. Li, Z. Zhao, A review of the state of health for lithium-ion batteries: research status and suggestions, J. Clean. Prod. 261 (Jul. 2020) 120813, https://doi.org/10.1016/j.jclepro.2020.120813.
[6] J. Lu, T. Wu, K. Amine, State-of-the-art characterization techniques for advanced lithium-ion batteries, Nat. Energy 2 (3) (Mar. 2017) 17011, https://doi.org/10.1038/nenergy.2017.11.
[7] M. Weiss, et al., Fast charging of lithium-ion batteries: a review of materials aspects, Adv. Energy Mater. 11 (33) (2021) 2101126, https://doi.org/10.1002/aenm.202101126.
[8] M. Finsterbusch, T. Danner, C.-L. Tsai, S. Uhlenbruck, A. Latz, O. Guillon, High capacity garnet-based all-solid-state lithium batteries: fabrication and 3D-Microstructure resolved modeling, ACS Appl. Mater. Interfaces 10 (26) (Jul. 2018) 22329–22339, https://doi.org/10.1021/acsami.8b06705.
[9] W.-Y.A. Lam, H. Zhao, B. Zhang, L. Wang, H. Xu, X. He, Significance of direct observation of lithium-ion distribution and potential distribution inside batteries through operando analyses, Next Energy 2 (Jan. 2024) 100106, https://doi.org/10.1016/j.nxener.2024.100106.
[10] M. Sina, et al., Direct visualization of the solid electrolyte interphase and its effects on silicon electrochemical performance, Adv. Mater. Interfac. 3 (20) (2016) 1600438, https://doi.org/10.1002/admi.201600438.
[11] S. Park, et al., Ionic conductivity and mechanical properties of the solid electrolyte interphase in lithium metal batteries, energymater 3 (1) (Feb. 2023), https://doi.org/10.20517/energymater.2022.65. N/A-N/A.
[12] A. Nakagawa, N. Kuwata, Y. Matsuda, J. Kawamura, Characterization of stable solid electrolyte lithium silicate for thin film lithium battery, J. Phys. Soc. Jpn. 79 (Suppl.A) (Jan. 2010) 98–101, https://doi.org/10.1143/JPSJS.79SA.98.
[13] S. Friedrich, et al., Effect of mechanical pressure on lifetime, expansion, and porosity of silicon-dominant anodes in laboratory lithium-ion cells, J. Electrochem. Soc. 171 (5) (May 2024) 050540, https://doi.org/10.1149/1945-7111/ad36e6.
[14] M. Wetjen, S. Solchenbach, D. Pritzl, J. Hou, V. Tileli, H.A. Gasteiger, Morphological changes of silicon nanoparticles and the influence of cutoff potentials in silicon-graphite electrodes, J. Electrochem. Soc. 165 (7) (May 2018) A1503, https://doi.org/10.1149/2.1261807jes.
[15] S. Möller, et al., A new high-throughput focused MeV ion-beam analysis setup, Instruments 5 (1) (Mar. 2021), https://doi.org/10.3390/instruments5010010. Art. no. 1.
[16] V. Paneta, A. Kafkarkou, M. Kokkoris, A. Lagoyannis, Differential cross-section measurements for the 7Li(p,p0)7Li, 7Li(p,p1)7Li, 7Li(p,α0)4He, 19F(p,p0)19F, 19F(p,α0)16O and 19F(p,α1,2)16O reactions, Nucl. Instrum. Methods Phys. Res. Sect. B Beam Interact. Mater. Atoms 288 (Oct. 2012) 53–59, https://doi.org/10.1016/j.nimb.2012.07.020.
[17] J.F. Ziegler, M.D. Ziegler, J.P. Biersack, SRIM – the stopping and range of ions in matter (2010), Nucl. Instrum. Methods Phys. Res. Sect. B Beam Interact. Mater. Atoms 268 (11) (Jun. 2010) 1818–1823, https://doi.org/10.1016/j.nimb.2010.02.091.
[18] K.F. Muzakka, et al., Analysis of Rutherford backscattering spectra with CNN-GRU mixture density network, Sci. Rep. 14 (1) (Jul. 2024) 16983, https://doi.org/10.1038/s41598-024-67629-y.
[19] J.L. Campbell, et al., The Guelph PIXE software package V, Nucl. Instrum. Methods Phys. Res. Sect. B Beam Interact. Mater. Atoms 499 (Jul. 2021) 77–88, https://doi.org/10.1016/j.nimb.2021.05.004.
[20] S. Möller, et al., Absolute local quantification of Li as function of state-of-charge in all-solid-state Li batteries via 2D MeV ion-beam analysis, Batteries 7 (2) (Jun. 2021), https://doi.org/10.3390/batteries7020041. Art. no. 2.
[21] D. Jantke, R. Bernhard, E. Hanelt, T. Buhrmester, J. Pfeiffer, S. Haufe, Silicon-Dominant anodes based on microscale silicon particles under partial lithiation with high capacity and cycle stability, J. Electrochem. Soc. 166 (16) (Nov. 2019) A3881, https://doi.org/10.1149/2.1311915jes.
[22] A. Durdel, S. Friedrich, L. Hüsken, A. Jossen, Modeling silicon-dominant anodes: parametrization, discussion, and validation of a newman-type model, Batteries 9 (11) (Nov. 2023), https://doi.org/10.3390/batteries9110558. Art. no. 11,.
[23] J. Kim, O.B. Chae, B.L. Lucht, Perspective—Structure and stability of the solid electrolyte interphase on silicon anodes of lithium-ion batteries, J. Electrochem. Soc. 168 (3) (Mar. 2021) 030521, https://doi.org/10.1149/1945-7111/abe984.
[24] S. Möller, M. Finsterbusch, K.F. Muzakka, MeV Ion beam analysis of granite in 10000 points, Zenodo (Oct. 17, 2024), https://doi.org/10.5281/zenodo.13944189.
[25] S. Möller, A. Durdel, L. Streck, K.F. Muzakka, M. Finsterbusch, 3 MeV Proton Ion beam analysis of NCA/Si anode-cathode mapping, Zenodo (Nov. 12, 2024), https://doi.org/10.5281/zenodo.14096284.
[26] M. Nie, D.P. Abraham, Y. Chen, A. Bose, B.L. Lucht, Silicon Solid Electrolyte Interphase (SEI) of lithium ion battery characterized by microscopy and spectroscopy, J. Phys. Chem. C 117 (26) (Jul. 2013) 13403–13412, https://doi.org/10.1021/jp404155y.
[27] S. Park, S. Kim, J.-A. Lee, M. Ue, N.-S. Choi, Liquid electrolyte chemistries for solid electrolyte interphase construction on silicon and lithium-metal anodes, Chem. Sci. 14 (37) (2023) 9996–10024, https://doi.org/10.1039/D3SC03514J.
[28] H. Nakai, T. Kubota, A. Kita, A. Kawashima, Investigation of the Solid Electrolyte Interphase Formed by Fluoroethylene Carbonate on Si Electrodes, J. Electrochem. Soc. 158 (7) (May 2011) A798, https://doi.org/10.1149/1.3589300.
[29] 'Analysis of transient current and heat flow during voltage holds: for 70 wt% silicon anode lithium-ion cells - IOPscience'. Accessed: October. 20, 2025. [Online]. Available: https://iopscience.iop.org/article/10.1149/1945-7111/ad940e.
[30] C. Xu, et al., Improved performance of the silicon anode for Li-Ion batteries: understanding the surface modification mechanism of fluoroethylene carbonate as an effective electrolyte additive, Chem. Mater. 27 (7) (Apr. 2015) 2591–2599, https://doi.org/10.1021/acs.chemmater.5b00339.
[31] L. Hartmann, et al., Depletion of electrolyte salt upon calendaric aging of lithium-ion batteries and its effect on cell performance, J. Electrochem. Soc. 171 (6) (Jun. 2024) 060506, https://doi.org/10.1149/1945-7111/ad4821.
[32] S. Haufe, J. Ranninger, R. Bernhard, I. Buchberger, E. Hanelt, Improving cycle life of silicon-dominant anodes based on microscale silicon particles under partial lithiation, Batteries 9 (1) (Jan. 2023) 58, https://doi.org/10.3390/batteries9010058.